Droplet Dynamics in Vertical Gas-Liquid Annular Flow

Data for the two-dimensional velocity and size of entrained drops carried by the gas core during upward annular gas liquid flow are presented. The measurements of velocity and size were made simultaneously using a new experimental technique. Information on the variation of the drop velocity with flow rates, radial position in the core, and drop size are presented and analyzed. Droplet velocity is shown to increase with size, counter to intuitive expectation. This is explained in terms of highly modified drag-Reynolds number relationships caused by the high turbulence level in the core.

J. C. B. Lopes, A. E. Dukler
Department of Chemical Engineering
University of Houston
Houston, TX

Introduction

During the simultaneous upward flow of gas and liquid in a vertical pipe a variety of flow patterns can exist. At high gas and low liquid flow rates an annular flow pattern is observed. Here part of the liquid flows upward along the wall as a thin, highly wavy film with the gas flowing in the core. The remainder of the liquid is carried by the gas phase in the form of drops. Conditions exist where a considerable fraction of the liquid feed is entrained, as shown by Ueda (1981), Zabaras *et al.* (1986), and others. The distribution of the liquid between the film and dispersed phase and the process of interchange as drops deposit into the film and new drops are created by the gas flow can have profound effects on transfer phenomena. Attempts to model these processes ignoring the role of the drops can lead to considerable error, as recently shown with respect to momentum transfer (Lopes and Dukler, 1986). The prediction of rates of deposition and the motion of the drops relative to the gas phase requires an understanding of the dynamics of the drop motion.

Experimental difficulties have resulted in few applicable studies in the literature. In order to obtain useful information it is necessary to simultaneously measure size and velocity of the individual drops in a fast-moving gas stream. Most earlier studies analyzed photographic records obtained from high-speed flash, cine film, or video tape. The difficulty in locating and tracking individual drops and the tedium of frame study resulted in relative few measurements for each condition. Therefore the statistical reliability of the data was low. This method averages the information over the tube cross-sectional area and over at least a few diameters of axial length. As a result, extracting data for local values is not possible. In these photographic methods only one component of the velocity was reported. Laser velocimetry methods have also been used. Here there is a special problem of optically penetrating the annular film. In addition, this method depends on the existence of Mie scattering, which is suppressed for the large drops observed in annular flow.

A summary of previously reported data can be found in Table 1, from which the very limited nature of this information can be discerned. In the present work simultaneous measurements were made of the size as well as the axial and radial components of the velocity vector along the radius in the gas core. This paper presents the velocity data and their dependence on flow conditions, radial position, and drop size. In an attempt to interpret the data, speculations are advanced for the nature of the interactions between the gas and drops in this highly turbulent gas core.

Droplet Velocity Measurements

Experimental technique

The annual flow experiments were conducted in a 10 m long vertical Plexiglas cylindrical pipe of 50.74 ± 0.18 mm ID. The fluids used were air and water, which were injected at the bottom of the column. Both temperature and pressure were monitored at the measuring location and experiments were run at superficial velocities in the ranges 14–25 m/s for the gas and 0.03–0.12 m/s for the liquid. The experimental measurements of droplet sizes and velocities were made at 8.9 m from the gas injection point, equivalent to a distance of 175 pipe diameters.

The simultaneous measurement of droplet diameter and two droplet velocity components was obtained by use of an optical laser technique originally developed by Semiat and Dukler (1981). A comprehensive description of the method applied to

The present address of J. C. B. Lopes is Schlumberger-Doll Research, Ridgefield, CT 06877-4108.

Table 1. Previous Experimental Work on Simultaneous Measurement of Droplet Size and Velocity in Annular Flow

Source	Geometry	Fluids	Tube Dia. *mm*	Exp. Technique	Velocity Measured	Gas Velocity Range *m/s*	No. of Data Points per Flow Condition	Drop Size Range *μm*
Cousins & Hewitt (1968)	Circular pipe	Air/water	9.5	Cine-film	Axial	28.5–49.7	max. 83	105–405
Ardron & Hall (1981)	Circular pipe	Steam/water	15	Videotape	Axial	5.5–13.4	max. 300	250–1,000
Yeoman *et al.* (1982)	Circular pipe	Air/water	10	Two-color L.D.A.	Axial	47	max. 1,000	max. 100
Tong *et al.* (1983)	Rod bundle square pitch	Steam/water	20*	Cine-film	Axial	15–24	max. 330	250–3,000
James *et al.* (1980)	Circular pipe	Air/water	22	Cine-film	Radial	24	30	170–1,150
Andreussi & Azzopardi (1981)	Circular pipe	Air/water	22	Cine-film	Radial	24	min. 50	300–1,000
Langner & Mayinger (1982)	Circular pipe	Vapor/R12	14	High-speed cine	Radial	4	40	100–1,000
Wilkes et al. (1983)	Circular pipe	Air/water	10	Cine-film	Radial	—	—	—

*Equivalent diameter for a four-rod flow cell

annual flow can be found in Lopes and Dukler (1986). With this technique, at a fixed radial position, for each droplet detected three simultaneous measurements were obtained: the droplet diameter, d, the droplet axial velocity in the direction of the gas flow, v_z, and the droplet radial velocity in a direction normal to the tube centerline, v_r.

For each experiment the number of drops sampled was large enough so that the 95% confidence interval limit was within 3% and 9% for the average axial and radial velocities, respectively. Measurements were made at three radial locations.

Axial velocity

Typical probability density data for the axial velocities as measured at the centerline are presented in Figure 1. The solid curves represent the best fit using a Gaussian model. Mean values of the axial velocity, v_z, appear in Figure 2, where it is seen that $\bar{v}_z$, is only weakly dependent on liquid rate.

The difference in velocity between the gas and the droplet phase determines the slip velocity, $U_S = U_G - \bar{v}_z$, and the slip ratio, S_R, defined as:

$$S_R = \frac{U_S}{U_G}. \tag{1}$$

While the local gas velocity was not measured in this study, its value at the axis, U_{G_0}, can be estimated from the universal velocity distribution law discussed by Schlichting (1979):

$$U_{G_0} = 3.75u^* + U_{GS} \tag{2}$$

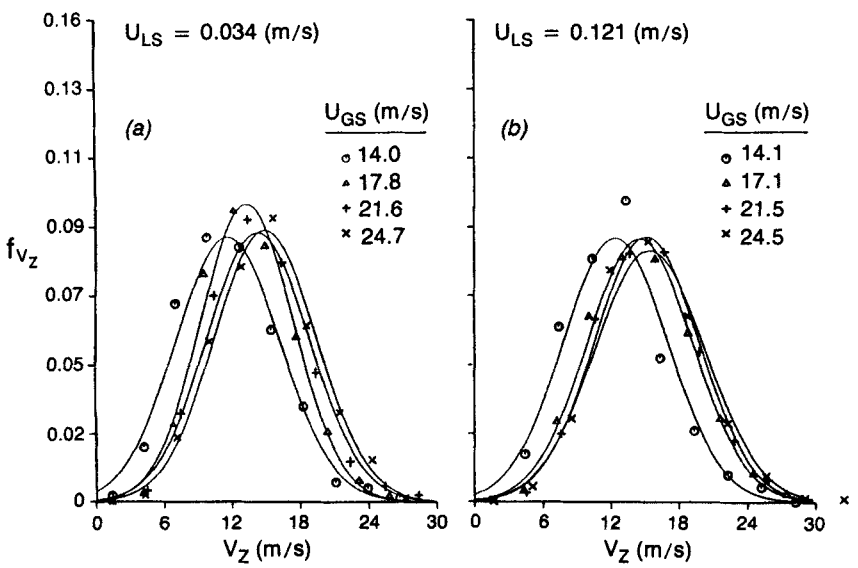

Figure 1. Probability density function for axial velocity.

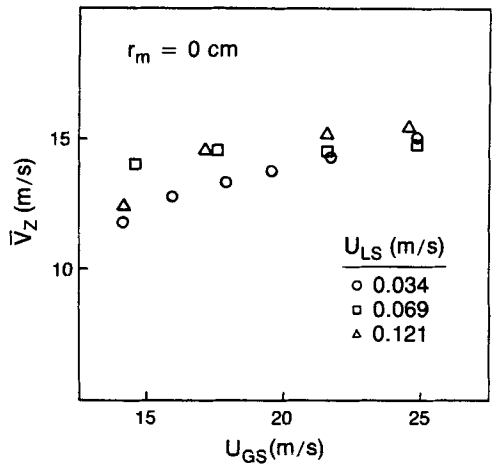

Figure 2. Average axial velocity at the centerline.

where u^* is the gas friction velocity and U_{GS} is the superficial gas velocity. This relationship is shown by Schlichting to be equally valid for smooth and rough pipes. The average slip velocity at the centerline, U_{S_0}, can be found from:

$$U_{S_0} = U_{GS} + 3.75u^* - \bar{v}_{z_0} \tag{3}$$

and the corresponding slip ratio by:

$$S_{R_0} = 1 - \frac{\bar{v}_{z_0}}{U_{GS} + 3.75u^*}. \tag{4}$$

For each experimental condition, measured values of pressure gradient and film thickness were used to calculate total momentum exchange with the interface. That portion due to droplet interchange was excluded in the manner discussed by Lopes and Dukler (1986) and the remainder used to compute the interfacial shear τ_i from which u^* was calculated. Equation 4 was then used to find S_{R_0}. The results, which appear in Figure 3, again show an insensitivity to liquid rate. Of importance is the fact that the slip is of the order of 50% of the gas rate, much larger than previously thought to exist.

From the experiments at different radial locations the average droplet velocities obtained are plotted against the measurement radial location, r_M, in Figure 4. These results reveal the presence of a velocity profile for $\bar{v}_z$, but one that is only weakly dependent on r. The lowest values of $\bar{v}_z$ are found near the wall. Nevertheless, the curvature of the profile is very small for all cases and its shape seems to be maintained for different values of U_{GS} and U_{LS}.

The large number of measurements made at each flow condition (500–700) permitted the use of conditional sampling analysis to explore the effect of size on the drop velocities. From each experimental flow condition a set of N samples was obtained. The droplets were then sorted into classes of droplets of mean diameter, $\bar{d}^c$. Each class was defined by dividing the observed maximum size range $\{0 < d \leq d_{max}\}$, into fifteen equal intervals. For each class, characterized by $\bar{d}^c$, the average class velocities, $\bar{v}_z^c$ and $\bar{v}_r^c$, were then computed.

Figures 5a through 5c present $\bar{v}_z^c$ vs. $\bar{d}^c$ at the centerline for three different values of U_{LS}, each over a range of U_{GS}. Typical data off the centerline can be found in Figures 6a through 6d. The unexpected results that emerge from these data are that axial velocities increase markedly with increasing drop size. The larger droplets move faster than the smaller ones. In fact, the relative effect of the drop diameter in some cases is stronger than that of the gas velocity which provides the driving force. This is consistent for all liquid rates. The standard deviations for the class average velocities were of the order of 3 m/s. Therefore, every drop with larger value of d does not necessarily travel faster than drops with smaller diameter, but on average this is true. Near the centerline the mean drop velocity approaches or exceeds the superficial velocity U_{GS}. However the local velocity at the centerline is approximately 1.4 U_{GS} as indicated by Eq. 2. Thus, the gas velocity exceeds the drop velocity at all radial locations, as is expected.

The dependence of $\bar{v}_z^c$ on U_{GS} is weak. This can be explained by the shape of the $\bar{v}_z^c$ vs. $\bar{d}^c$ curves. Figure 7 shows curves of $\bar{v}_z^c$ vs. $\bar{d}^c$ for a given U_{LS} and two values of U_{GS}, along with probability density distributions of the drop sizes for each flow rate. An increase in the gas rate results in a shift to smaller drop sizes. The smaller drop sizes travel at lower velocities. Thus, the average velocity is lower than it would be if the size distribution remained unchanged as the gas rate increases.

It is interesting to observe that for the position closest to the wall, r_M = 2.0 cm (Figures 6b and 6d), the curve $\bar{v}_z^c$ vs. $\bar{d}^c$ passes

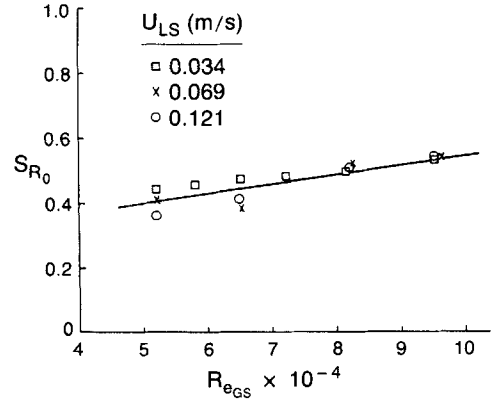

Figure 3. Experimental slip ratio vs. gas Reynolds number at centerline.

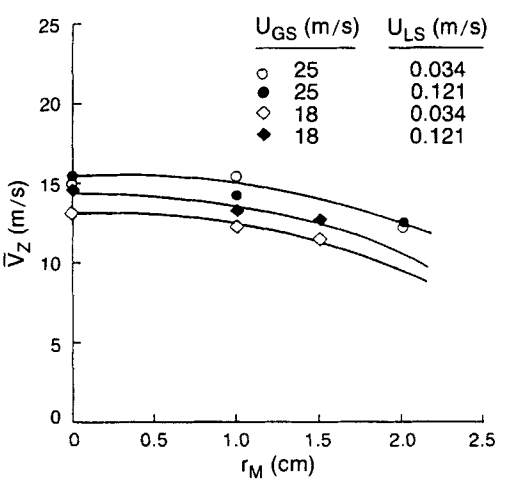

Figure 4. Average droplet axial velocity radial profiles for different flow rates.

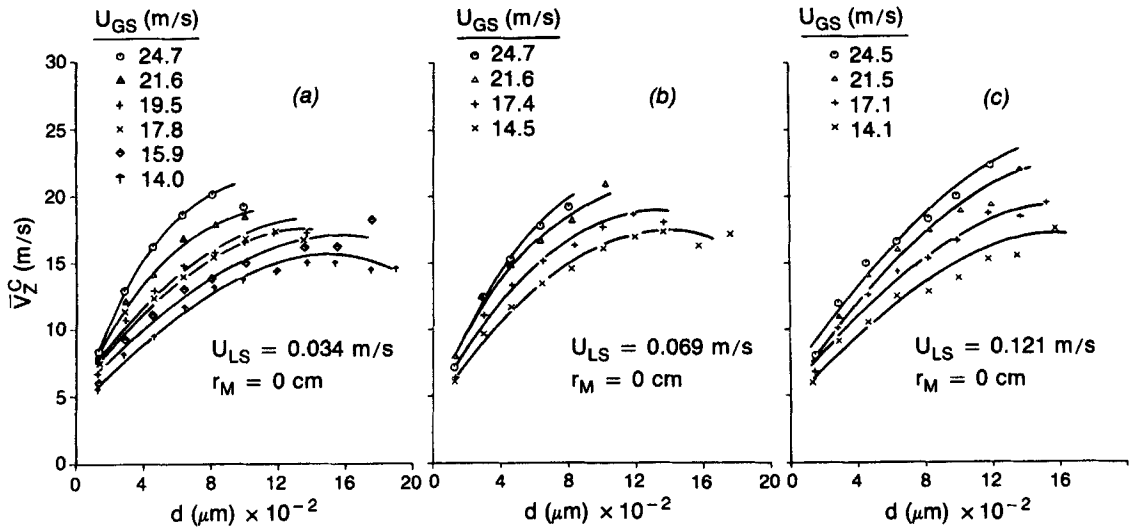

Figure 5. Experimental droplet axial velocity vs. droplet size for different liquid and gas rates at centerline.

through a maximum, i.e., the large particles that are fastest at the center position are not necessarily the fastest closer to the wall. However, as they move toward the center these large droplets undergo the biggest increase in velocity compared to the other sizes. This reveals that they are under the influence of larger accelerations than those of the smaller drops. This effect will be analyzed in a section below.

Radial velocity

The mean lateral velocity of the drops is zero as a result of the axial symmetry. However, of interest is the mean radial velocity $\bar{v}_r$. This appears in Figure 8 as a function of the dimensionless gas rate, Re_{GS}, for all the radial positions. The values are much smaller than mean axial velocities measured for the same conditions and are essentially constant and independent of liquid rates and radial position.

Andreussi and Azzopardi (1981), following a suggestion made by Tatterson (1975), speculated that the kinetic energy of the droplet is proportional to the work done by the gas pressure forces on the wave as the drop is formed. The result is that $\bar{v}_r$ is proportional to the friction velocity u^*. This was confirmed by Wilkes et al. (1983) working with a different pipe size. In this

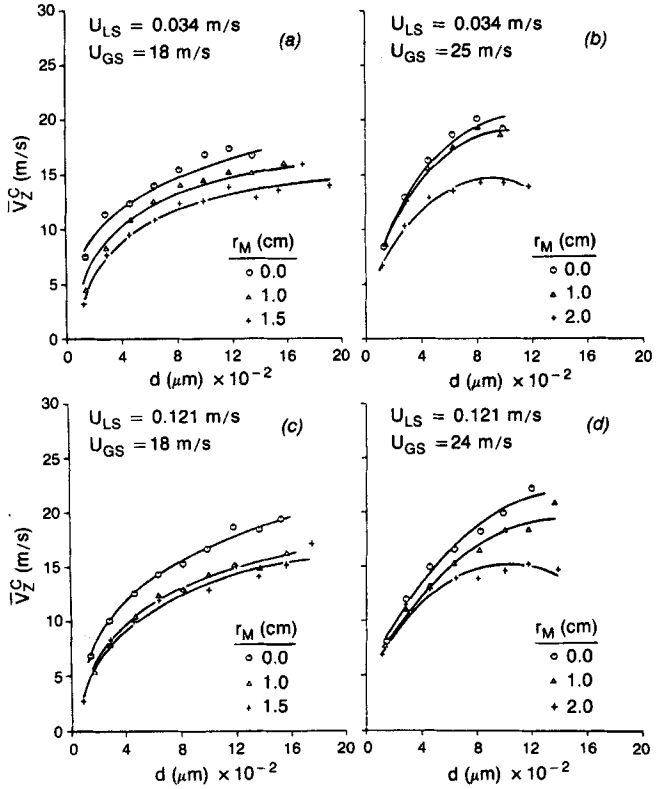

Figure 6. Experimental droplet axial velocity vs. droplet size for different gas and liquid rates and varying radial position.

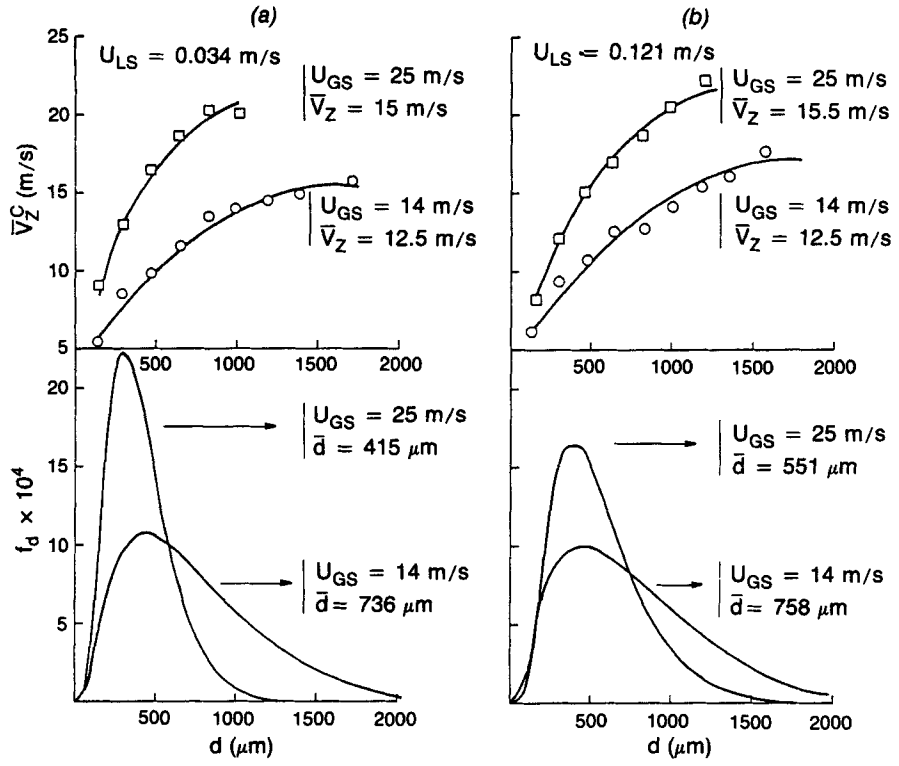

Figure 7. Simultaneous droplet axial velocities and droplet size distributions for different liquid and gas rates.

study the values of u^* based on the interfacial shear and gas density varied only between 1.9 and 2.0 m/s for the full range of gas and liquid rates. Thus the constancy of $\bar{v}_r$ is consistent with earlier work.

This independence of average radial velocity with radial position suggests that the lateral velocity of the droplet is constant along the droplet flight path. The analysis of the class averages of the radial velocity, $\bar{v}_r^c$, revealed an almost constant value of $\bar{v}_r^c$ for all values of $\bar{d}^c$. This is in agreement with the results of Andreussi and Azzopardi and reinforces the idea that in annular flow the radial velocity of droplets of this size range is mainly controlled by the velocity at which the droplets are ejected from the waves. The constancy of $\bar{v}_r^c$ also implies that the droplets have, on average, the same flight times, independent of their sizes.

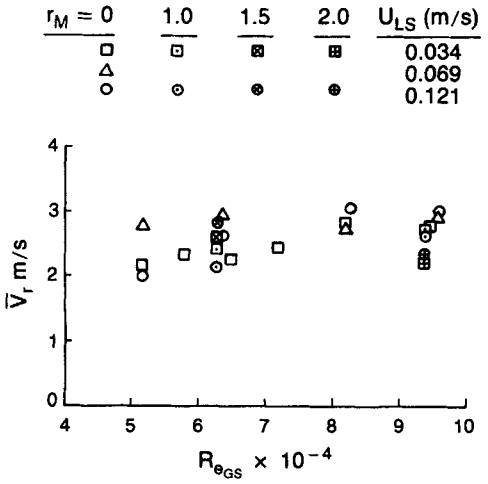

Figure 8. Dependence of average radial velocity on flow rates and radial position.

Equation of Motion of Droplets in Annular Flow

Consider a liquid droplet of volume V and density ρ_l, at any arbitrary time t, traveling through a gas of density ρ_g, which experiences a frictional pressure gradient, ∇p, as a result of its flow. Assuming no mass transfer between phases, the following equation of motion applies to the droplet:

$$\frac{d}{dt}\underline{v} = \left(\frac{1-\gamma}{\gamma}\right)g\underline{k} - \frac{1}{\rho_l}\nabla p + \frac{1}{V_{\rho_l}}\underline{F}_D \qquad (5)$$

where $\underline{v}$ is the droplet velocity vector relative to a fixed frame of reference, γ is the liquid-gas density ratio ρ_l/ρ_g, g is the acceleration of gravity, $\underline{k}$ is the unit vector pointing upward in the vertical direction and $\underline{F}_D$ is the net drag force on the droplet resulting from the relative motion of the gas and liquid. The velocity and position of the particle as a function of time can be found by double integration of Eq. 5. For this purpose $\underline{F}_D$ must be specified.

The extensive research leading to an understanding of $\underline{F}_D$ has been summarized by Clift et al. (1978). Most of the results that appear in the literature have been based on measurements made under conditions of steady motion in fields of low turbulence intensity. However, in two-phase annular flow the velocity fluctuations in the gas core are high, consistent with the large values of the interfacial shear that have been measured. High turbulence intensities are known to have profound effects on the transition and separation in boundary layers, as will be discussed below. Thus they can be expected to influence the particle drag.

Drag force

The classical equation by Basset, Boussinesq, and Oseen (BBO) provides a general relationship for the drag force, F_D, during creeping motion of an accelerating particle as it passes through a stagnant fluid. Odar and Hamilton (1964) suggested that the equation could be extended to higher velocities by replacing the drag coefficient for Stokes flow with the true drag coefficient, C_D. In the presence of a flowing gas stream this relation can be further generalized to include the relative velocity. The result is:

$$-F_D = \frac{3}{4} C_D \frac{V\rho_g}{d} |v_R| v_R + \frac{1}{2} \rho_g V \frac{d}{dt} v_R + \frac{3}{2} d^2 (\pi \rho_g \mu_g)^{1/2} B(t) - \rho_g V \frac{d}{dt} U_G \quad (6)$$

where $B(t)$ is the Basset integral, given by:

$$B(t) = \int_{-\infty}^{t} \left(\frac{d}{dt} v_R\right)_{t=s} (t - s)^{-1/2} \, ds \quad (7)$$

where $v_R = v - U_G$ is the droplet relative velocity, and ρ_g and μ_g are the density and viscosity of the gas, respectively. The first term in Eq. 6 corresponds to the drag for the steady motion, the second is the added mass term, the third is the Basset term accounting for added drag due to velocity of the particle along its path. The last term is the extra force necessary to accelerate the fluid that would occupy V if the particle were absent. For the case of liquid drops in low-density air the last three terms in Eq. 6 are negligible compared to the first. Then, Eq. 6 can be simplified and extended to three-dimensional motion through the following expression:

$$-\underline{F}_D = \frac{3}{4} C_D \frac{V\rho_g}{d} \|\underline{v}_R\| \underline{v}_R \quad (8)$$

where C_D is computed at a Reynolds number Re with the relative speed $\|\underline{v}_R\|$. The simplification that C_D be calculated at v_{R_i}, the ith component of $\underline{v}_R$ can lead to significant error for $Re > 1$, although correct in Stokes flow (Rudinger, 1974).

Replacing Eq. 8 in the equation of motion, Eq. 5, results in:

$$\frac{d}{dt} \underline{v} = \left(\frac{1 - \gamma}{\gamma}\right) g\underline{k} - \frac{1}{2} \frac{1}{\rho_l} \nabla p - \frac{3}{4} \frac{C_D}{\gamma d} \|\underline{v}_R\| \underline{v}_R \quad (9)$$

where $\underline{v}_R = \underline{v} - \underline{U}_G$. In Eq. 9 the total droplet acceleration is given by the sum of three acceleration terms:

- The gravitational acceleration that is constant for incompressible gas flow.
- The gas frictional pressure gradient acceleration that depends on the gas flow rate through the conduit. While the local values may vary due to the turbulent motion of the gas, the time average vertical component of the pressure gradient, $\nabla_z \bar{p}$, is constant over a cross section of the column.
- The drag acceleration.

Drag coefficient curves

The widely used standard drag curve shown in Figure 9 is a fit to experimental C_D data obtained for solid nonrotating spheres moving at terminal velocity through an unbounded quiescent fluid. The nature of the flow around the sphere changes with Reynolds number and it is useful to summarize what appears to be known:

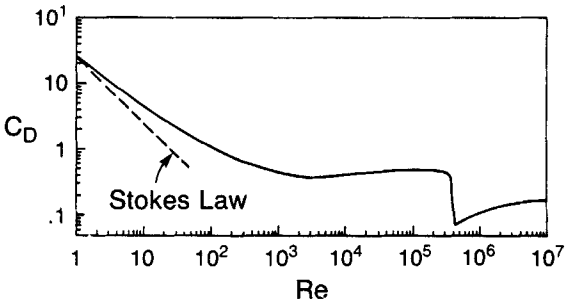

Figure 9. Standard drag curve.

- $0 < Re < 20$: A laminar boundary layer surrounds the body and viscous forces dominate. Separation occurs close to $Re = 20$ near the rear stagnation point, and as a result the form drag begins to contribute to the total drag.
- $20 < Re < 10^3$: The separation point moves toward the front of the sphere and the form drag increases relative to skin friction. At $Re = 130$ the wake is no longer stable and vortex shedding starts. The drag curve starts to level out. At $Re = 150$ the form drag equals the skin drag and exceeds it from that point on. For $Re > 400$, vortex shedding starts from alternate sides of the sphere and the wake continues to grow in length with little change in width.
- $10^3 < Re < 3.2 \times 10^5$: Over this Newton's law region the drag coefficient is about constant at $C_D = 0.44$. As the upper limit is approached the laminar boundary layer has receded to a separation point located about 83° from the front stagnation point.
- $3.2 \times 10^5 < Re < 4 \times 10^5$: Catastrophe occurs and C_D quickly drops to its lowest value. This occurs because the attached portion of the boundary becomes turbulent and after separation it reattaches to the surface of the sphere at about 130° from the front, forming a large separation bubble. The form drag reduces as a result of the smaller wake. Dryden et al. (1937) defined the critical Reynolds number, Re_c, as the value at which C_D first reaches a value of 0.3 as it decreases, and this has been the generally accepted defintion. With further increases in Re past the critical, the separation bubble decreases until it disappears when C_D is a minimum.
- $Re < 4 \times 10^5$: Further increase in Re moves the separation point toward the front with increase in the form drag.

Data from annular flow experiments reported here show that $10 < Re < 10^3$ is a region where C_D decreases with Re according to the standard curve. Use of this curve for C_D in Eq. 9 predicts that the small particles move faster than the larger ones, a result contrary to experiment. It would appear that during annular flow the situation could be significantly different from that predicted by the standard curve for three possible reasons:

a. The drops are not spherical, the condition on which the data of Figure 9 are based.

b. The acceleration experienced by the drops causes changes in C_D.

c. The existence of a turbulent carrier fluid rather than an undisturbed one causes significant changes in the drag curve.

Photographic studies by Cousins and Hewitt (1968) and Langner and Mayinger (1982) show that in upward annular

flow even the largest of drops is remarkably spherical. There have been numerous studies on the effect of acceleration on drag (Torobin and Gauvin, 1961; Marchildon and Gauvin, 1979; Temkin and Mehta, 1982) with conflicting results. Even for the largest reported effects it is possible to conclude that the influence of the acceleration on drag is not large enough to explain the behavior observed in the annular flow experiments.

A substantial circumstantial case can be made for the speculation that the characteristics of the turbulence have a large influence on the drag coefficient. It has long been known (Schlichting, 1979) that even low levels of turbulent intensity in the free stream can result in large changes in the Reynolds number at which the boundary layer transition to turbulence takes place. Since the sharp drop in C_D for spheres is associated with such a transition as discussed above, turbulent intensity should influence the value of the critical Re at the "crisis" and it has, indeed, been observed (Dryden et al., 1937; Torobin and Gauvin, 1961; Clamen and Gauvin, 1969; Neve et al., 1986. Taylor (1936) argued that the relationship between the Eulerian macroscale and the particle diameter payed a key role, and Neve (1986) appears to show some scale effects for measurements on large spheres made behind large grids. While the influence of the large-scale structure of the turbulence can be expected to have an effect on large spheres, it seems unlikely to be important for the drops considered here, which are less than 2,000 μm in diameter. Gauvin, in his several papers likewise discounts the possibility that scale has any importance.

All of these considerations suggest a strong dependence of the C_D–Re curve on the relative turbulence intensity, I_R:

$$I_R = \frac{u_{rms}}{v_R}. \tag{10}$$

u_{rms} being the root mean square turbulent gas velocity. Previous investigators have studied the effect of turbulence over various ranges of the C_D–Re curve. Therefore in order to evolve a coherent picture of the effect of I_R, which would be useful for computation, it is necessary to construct a piecewise description from several studies. Figure 10 is such a description for a constant I_R where the different ranges are defined by results of different investigators. For each range the applicable equations are as follows:

$$\log_{10} Re_c = 5.477 - 15.8 I_R \quad \text{for } I_R \le 0.15 \tag{11}$$

$$\log_{10} Re_c = 3.371 - 1.75 I_R \quad \text{for } I_R > 0.15 \tag{12}$$

$$\log_{10} Re_M = 6.878 - 23.2 I_R \quad \text{for } I_R \le 0.15 \tag{13}$$

$$\log_{10} Re_M = 3.663 - 1.77 I_R \quad \text{for } I_R > 0.15 \tag{14}$$

$$Re_V = \left[Re_c^3 Re_M^{(0.45+20I_R)} \right]^{1/(3.45+20I_R)} \tag{15}$$

and

$$C_D = 162 I_R^{1/3} Re^{-1} \quad \text{for } 0.05 \le I_R \le 0.5 \text{ and } 10 < Re < 50 \tag{16}$$

$$C_D = 0.133(1 + 150 Re^{-1})^{1.565} + 4 I_R \quad \text{for } 0.07 \le I_R \le 0.5 \text{ and } 50 < Re < 700 \tag{17}$$

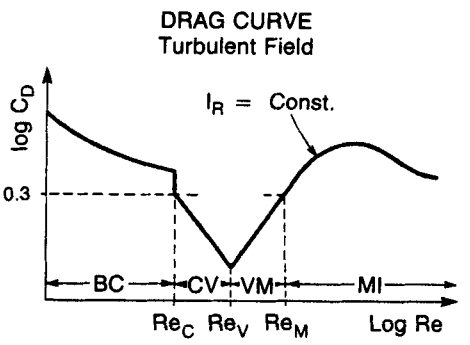

Figure 10. Schematic particle drag curve for a fixed level of turbulence.

$$C_D = 0.3(Re/Re_c)^{-3} \quad \text{for } 0.9 Re_c \le Re \le Re_V \tag{18}$$

$$C_D = 0.3(Re/Re_M)^{(0.45+20I_R)} \quad \text{for } Re_V \le Re \le Re_M \tag{19}$$

$$C_D = 3{,}990\,(\log_{10} Re)^{-6.1} - 4.47 \times 10^5 I_R^{-0.97} Re^{-1.8} \quad \text{for } I_R \ge 0.07 \text{ and } Re_M \le Re \le 3 \times 10^4 \tag{20}$$

$$C_D = \frac{24}{Re}(1 + 0.15 Re^{0.687}) + \frac{0.42}{(1 + 4.25 \times 10^4 Re^{-1.16})} \quad \text{for } I_R < 0.07,\ Re \le 10^5. \tag{21}$$

Equations 11–15 were suggested by Clift and Gauvin (1971), Eqs. 16–17 by Uhlerr and Sinclair (1970), Eqs. 18–20 by Clift and Gauvin (1971), and Eq. 21 by Clift and Gauvin (1970).

These empirical equations display discontinuities in some cases where they intersect, as shown by the solid line in Figure 10. Clearly the actual curves must be continuous. In order to eliminate these discontinuities to permit use of these data in numerical algorithms, the individual branches were matched at their intersections. As a result, changes were made to some of the above equations as follows. The limits on Equation 17 become:

$$\text{for } 0.07 \le I_R \le 0.5 \text{ and } 50 < Re < \min\{0.9 Re_c, 700\}$$

and a correction factor C_C is introduced into Eq. 20:

$$C_D = 3{,}990\,(\log_{10} Re)^{-6.1} - 4.47 \times 10^5 (I_R + C_C)^{-0.97} Re^{-1.8} \tag{22}$$

where

$$C_C = k_1 \exp(k_2 I_R Re + k_3 Re) I_R^{k_4} \tag{23}$$

and the constants assume the following values:

$$k_1 = 2.42$$
$$k_2 = -6.01 \times 10^{-3}$$
$$k_3 = -2.90 \times 10^{-3}$$
$$k_4 = -2.72 \times 10^{-1}.$$

With these adjustments, there now is in place a consistent set of equations with which drag coefficients can be estimated from the Reynolds number. Figure 11 shows the drag curves obtained

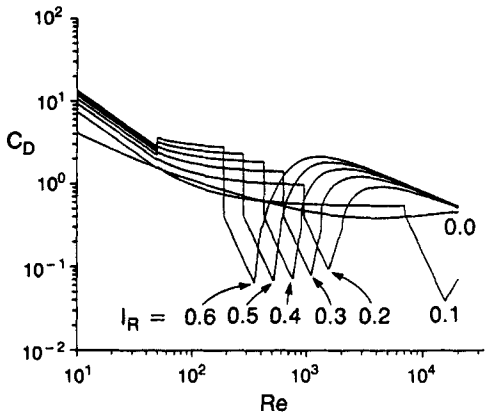

Figure 11. Particle drag curves for different levels of turbulence.

in this way for various values of I_R. These can be used in Eq. 9 to calculate the dynamic behavior of the drops in annular flow.

Droplet terminal velocity

The terminal velocity for the droplet is achieved when the forces acting on it are in balance. When the pressure gradient contribution is negligible, and for vertical rectilinear motion, Eq. 9 reduces to:

$$(\gamma - 1)g + \frac{3}{4}\frac{C_D}{d}|v_{R_T}|v_{R_T} = 0. \tag{24}$$

The solutions of this equation, for the case of water droplets in air at atmospheric pressure, are plotted in Figure 12a using the standard drag curve. In this case with $I_R = 0$, the smallest droplets will travel faster than the larger ones at equilibrium.

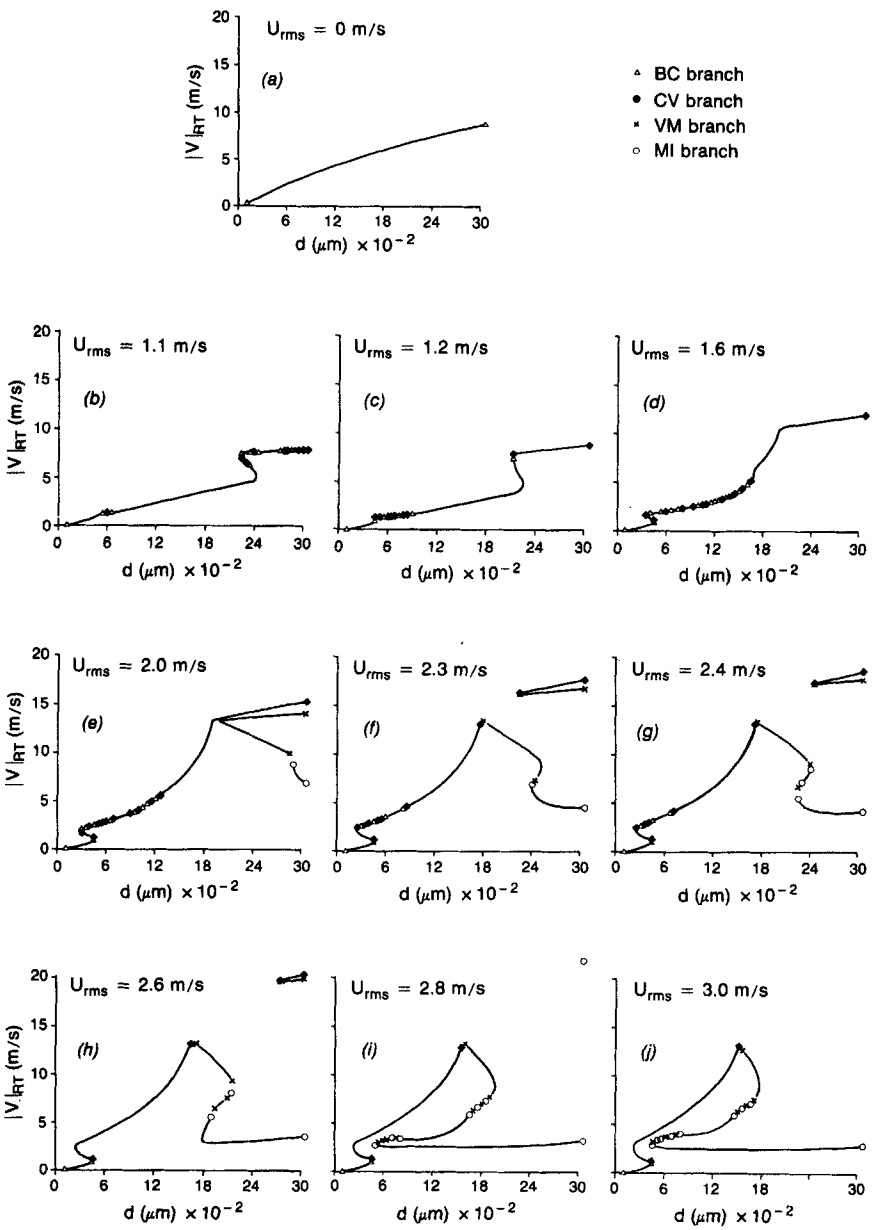

Figure 12. Bifurcation diagrams of terminal velocity vs. droplet size for different levels of turbulence.

For $I_R \neq 0$, a systematic search for solutions of Eq. 24 using the drag curve defined by Eqs. 11–23 was performed. For every diameter increment of 50 μm over the range $0 < d < 3{,}000$ μm, the existence of solutions was determined numerically for each 0.1 m/s interval of terminal velocity in the range of 0 to 30 m/s. The results are plotted in Figures 12b through 12j in the form of $|v_{R_T}|$ vs. d for selected values of the turbulence intensity, u_{rms}. For certain values of d, and at fixed u_{rms}, there are multiple values of v_{R_T} that satisfy Eq. 24. The multiplicity degree is always an odd number, being 1, 3, or 5. Furthermore, it is no longer always true that larger diameters correspond to higher terminal velocities. Each point in Figures 12a through 12j is identified with the particular branch of the drag curve where the drag coefficient is found for that terminal velocity (see Figure 10).

The values of u_{rms} selected for these curves represent typical bifurcation diagrams found. The evolution of these diagrams with increasing values of u_{rms} can be described as follows:

- $0.0 < u_{rms} \leq 0.9$: A single-valued solution curve is found similar to that found for $I_R = 0$ in Figure 12a.
- $0.9 < u_{rms} \leq 1.1$: The first multivalued region appears in the solution of multiplicity three, forming a bifurcation diagram of the hysteresis type, Figure 12b.
- $1.1 < u_{rms} \leq 1.5$: A second region of multiplicity three appears, of the same hysteresis type, at lower values of d, Figure 12c.
- $1.5 < u_{rms} \leq 1.6$: The region of multiplicity three at higher values of d unfolds and a single multivalued region is maintained, Figure 12d.
- $1.6 < u_{rms} \leq 2.0$: A new multivalued region of multiplicity three shows at larger values of d but with three branches. This region consists of a top branch from the preceding diagram and underneath it a finger-type branch, constituting an isola-type bifurcation. This finger moves upward as u_{rms} increases and touches the top branch at $u_{rms} = 2$, Figure 12e.
- $2.0 < u_{rms} \leq 2.3$: A new finger branch is created at the top region of the diagram with the same upward trend with u_{rms}. The branch below the finger folds on itself, forming a new kind of bifurcation diagram of the mushroom type, and a region of multiplicity five appears for the first time, Figure 12f.
- $2.3 < u_{rms} \leq 2.4$: The finger moves further to the top and right region of the diagram, finally causing the region of multiplicity five to disappear, Figure 12g.
- $2.4 < u_{rms} \leq 2.7$: Three regions of multiplicity three can be found, Figure 12h.
- $2.7 < u_{rms} \leq 2.9$: The folding of the lower branch for larger particles continues and two regions of multiplicity three are present, Figure 12i.
- $2.9 < u_{rms} \leq 5$: A new region of multiplicity five can be found for the lower particle size range. Meanwhile, the top finger has moved out of the diagram region, Figure 12j.

The possible existence of multiple solutions raises the problem of the stability of such solutions. This problem can be analyzed by recasting Eq. 24 in terms of forces and examining whether they are in a stable or unstable equilibrium when they are in balance. The ratio of the gravity force F_G to the drag force F_D is then expressed as:

$$\frac{F_D}{F_G} = \frac{C_D\left(\frac{1}{2}\rho_f|v_R|v_R\right)\pi d^2}{4(1-\gamma)gV} = g_R(v_R), \qquad (25)$$

where $g_R(v_R)$ is a function that takes the value one, whenever $v_R = v_{R_T}$. In Figure 13 this function is shown for $u_{rms} = 4.5$ m/s and for three different sizes. For the two smaller values of d, the function $g_R(v_R)$ takes the value one for three different values of v_{R_T}, but at the largest d size takes a value of one only once. Consider the curve for $d = 750$ μm. There are three points, S_1, U_2, and S_3, where g_R takes the value one. The stability of each point can be inspected by analyzing the behavior of g_R around each of these points.

Around the point S_1, the behavior of g_R is as follows: if $|v_R|$ is increased, then g_R is greater than one, which means that the drag force is greater than the gravity force. Consequently v, the particle velocity, will increase with a consequent decrease of $|v_R|$. Thus the droplet has the tendency to return to S_1 and the point is stable. If $|v_R|$ is decreased below V_{R_T} at S_1, the drag force is smaller than the gravity force and the particle decelerates, v decreases, $|v_R|$ increases, and the condition returns to S_1. This behavior is associated with the positive slope of g_R at S_1. Since S_3 presents the same positive slope, S_3 behaves like S_1 and they both qualify as stable.

Around point U_2 the following is observed: if $|v_R|$ is increased, g_R is less than one, i.e., the gravity force is greater than the drag force, therefore the particle will accelerate, hence decreasing $|v_R|$ with time and moving away from U_2. The same behavior is observed for a decrease in $|v_R|$ by similar arguments. Then, in this case, the point U_2 qualifies as unstable.

This type of stability analyis, by inspection of the function $g_R(v_R)$, can be carried out over all the regions of multiplicity, with the uniform conclusion that the intermediate branches of the solution are unstable.

For certain regions of the curves, the branches are so close that for variations in U_G on the order of u_{rms}, the droplet velocity v_{R_T} can jump from one stable branch to another. Consider a droplet of 1,000 μm in an annular flow field with $u_{rms} = 3.0$ m/s, Figure 12j. Assume that the particle achieved the largest of the three possible terminal velocities predicted. At this condition, say the particle velocity is v. Turbulent gas flow is accompanied by significant fluctuations in velocity. As eddies having different velocities sweep across the particle, the relative velocity changes. For example, if the local gas velocity increases the value of v_R will decrease, and the point moves down in the bifurcation diagram, eventually crossing the unstable branch. The reverse situation is also possible. This implies a stochastic pro-

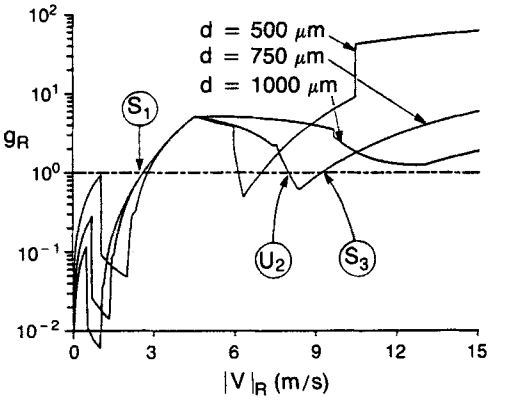

Figure 13. Bifurcation diagrams of terminal velocity vs. droplet size for different levels of turbulence.

cess suggesting that a single measurable v_{R_T} may not exist. Torobin and Gauvin (1961) found very large scatter in the values of C_D calculated from measured values of v_R for conditions of Re close to Re_c. Clift and Gauvin (1971) mention the possible existence of multiple solutions for v_{R_T}, but the problem was never analyzed.

This stability analysis can only describe the behavior close to equilibrium. In the section that follows an attempt is made to predict the velocities by integration of the equation of motion for comparison with the experimentally measured velocities at the centerline.

Droplet flight velocity

During annular flow over 95% of the entrained mass, flow is carried in drops that are greater than 200 μm in diameter (Lopes and Dukler, 1986). For drops of this size the criteria of Lumley (1957) can be used to show that turbulent fluctuations have negligible influence on the drop motion, the drops moving in a near-linear trajectory after the initial acceleration period (Lopes and Dukler, 1986). This has been confirmed by visual experiments by Cousins and Hewlett (1968) and Andreussi (1981). As the drop is released from the annular film its initial axial velocity, v_{z_0}, is assumed to be the velocity of the interfacial waves. Experiments by Zabaras (1985) in the same test section at similar gas and liquid rates showed that the wave velocity was about 3 m/s. The radial velocity, v_r, is constant at its ejection velocity, as presented above. For purposes of these calculations the gas velocity was assumed constant at its centerline value, $1.4U_{GS}$. A convenient way to solve Eq. 9 subject to these conditions is to use its integral form:

$$t - t_0 = \int_{v_{z_0}}^{v_z(t)} \frac{dv_z}{\left(\frac{1-\gamma}{\gamma}\right)g - \frac{1}{\rho_l}\nabla_z\bar{p} - \frac{3}{4}\frac{1}{\gamma d}C_D(Re, I_R)\|\underline{v}_R\|v_{Rz}}, \quad (26)$$

where $Re = (d\|\underline{v}_R\|/v_g)$ and $I_R = (u_{rms}/\|\underline{v}_R\|)$. In this way a quadrature procedure can be applied to evaluate the integral without any numerical problems due to discontinuities in the approximate expressions for C_D as given by Eqs. 11–23. For solution, the values of d, v_{z_0}, and v_r are selected. Equation 26 is solved by quadrature to obtain a series of values of v_z that correspond to a series of values of t. This process is continued until $t = t_F$, the time of flight between the interface and the centerline given by:

$$t_F = \left(\frac{D}{2v_r}\right), \quad (27)$$

where D is pipe diameter.

The values of v_z corresponding to t_F can be compared with the measured centerline axial velocities shown in Figure 5. The results of this integration are presented in Figure 14 as function of drop diameter, d. A constant pressure gradient of $\nabla_z\bar{p} = -550$ N/m^3 was used. Calculations were executed for u_{rms} varying from 0 to 10 m/s using the set of Eqs. 11–23 to compute the drag coefficient.

For zero turbulent intensity the calculated axial velocity at the centerline decreases monotonically. With increasing turbulence levels the velocity first decreases at low d and then displays

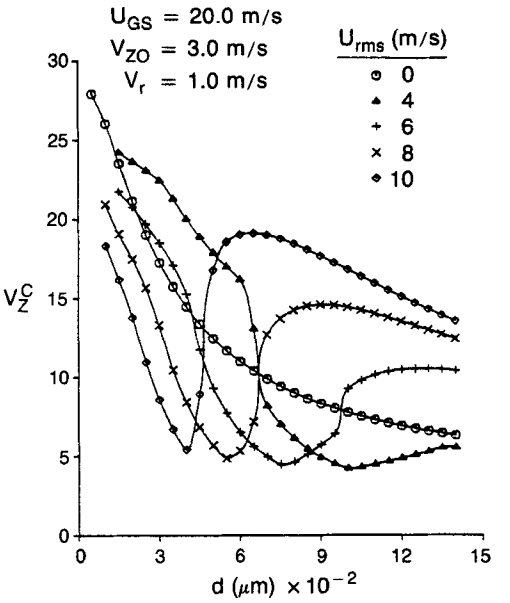

Figure 14. Axial velocity vs. droplet size predictions at centerline for different levels of turbulence.

a large region of increasing v_z with increasing diameter, just as observed in the experimental data presented in Figure 5. At higher values of d the velocity reaches a maximum after which it decreases again with increasing size. This effect is also suggested by at least some of the data.

The location of the minimum that occurs at low d is associated with the drag crisis and the value of Re_c at which it takes place. As the critical Reynolds number decreases, so will the value of d at which the minimum is observed. The movement of the large drops is controlled by the drag coefficient in the supercritical region of its curve, while the velocity of the small drops is determined by the subcritical portion. Thus the location of the critical point is important to the degree of quantitative comparison that can be expected. For example, Torobin and Gauvin (1961) suggested the following relation between Re_c and intensity I_R:

$$Re_c = \frac{45}{I_R^2} \quad (49)$$

which predicts lower values of the critical than do Eqs. 11 and 12. The various branches of the C_D–Re curves were shifted to fit this new critical and the velocity curves recalculated; the results appear in Figure 15. Still closer agreement is observed. While the trend is consistent with that observed experimentally, in order to get approximate quantitative agreement it is necessary to assume that the turbulent fluctuations can average as much as 40 to 50% of the gas velocity. In the presence of a highly agitated gas-liquid interface and as a result of the wakes created by the presence of the drops, these turbulence levels do not appear to be unreasonable. Kada and Hanratty (1960) found similar high values of turbulence for turbulent flow in pipes entraining small glass spheres. Low sphere concentrations could produce a 2.5-fold increase in the turbulent diffusion. However, a full test of the speculations presented here awaits the measurement of drag coefficients for drops or particles in situations where the relative turbulence intensity is comparable to that which exists

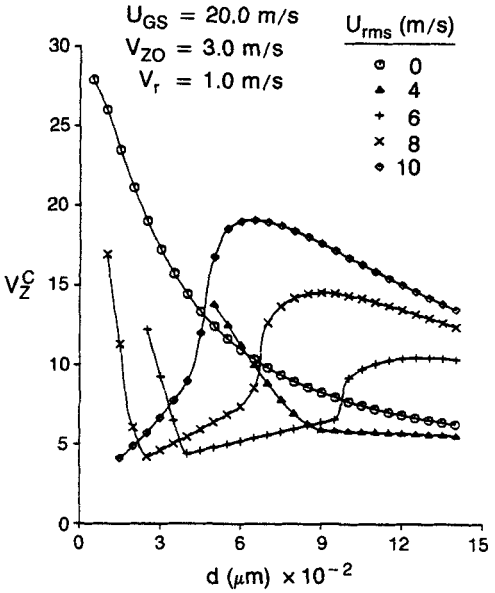

Figure 15. Axial velocity vs. droplet size predictions at centerline with modified drag curves at different levels of turbulence.

during annular flow. Such measurements are now in progress and will be reported in due course.

Acknowledgment

This work was made possible by the financial support of the Nuclear Regulatory Commission and the National Science Foundation.

Notation

C_D = drag coefficient
d = droplet diameter
d_{max} = maximum droplet diameter
D = column diameter
f_{v_z} = number-axial velocity probability density function
F_D = drag force
F_G = gravity force
g = acceleration of gravity
g_R = force ratio function, Eq. 25
I_R = relative turbulence intensity
$\underline{k}$ = vertical unit vector
r = radial coordinate
r_M = radial coordinate of measurement point
Re = droplet Reynolds number
Re_c = droplet critical Reynolds number
Re_{GS} = gas Reynolds number $\rho_g U_{GS} D/\mu_g$
Re_M = Re parameter, Eq. 13
Re_V = Re parameter, Eq. 15
S_R = slip ratio
S_{R_0} = slip ratio at centerline
t_F = time of droplet fight
u^* = friction velocity of gas phase $(\tau_i/\rho_g)^{1/2}$
u_{rms} = root mean square turbulent gas velocity
U_G = average axial velocity of gas in gas core
U_{GS} = superficial gas velocity $4W_G/(\rho_g \pi D^2)$
U_{G_0} = axial velocity of gas at centerline
U_{LS} = superficial liquid velocity $4W_L/(\rho_l \pi D^2)$
U_S = gas slip velocity
U_{S_0} = gas slip velocity at centerline
v_r = droplet radial velocity
v_R = relative droplet velocity
v_{R_T} = relative droplet terminal velocity
v_z = droplet axial velocity
v_{z_0} = droplet axial velocity at centerline
V = droplet volume
W_G = gas mass flow rate
W_L = liquid mass flow rate
z = vertical coordinate

Greek letters

γ = density ratio, ρ_l/ρ_g
μ_g = gas viscosity
τ_i = interfacial shear stress
ρ_g = gas density
ρ_l = liquid density
∇_p = pressure gradient
$\nabla_z p$ = z-component of pressure gradient vector

Superscripts

$\bar{x}$ = mean or average value of variable x
x^c = class value of variable x

Subscript

$\underline{x}$ = denotes variable x as a vector

Literature cited

Andreussi, P., "Droplet Transfer in Two-Phase Annular Flow," *Int. J. Multiphase Flow*, **9**, 697 (1983).

Andreussi, P., and B. J. Azzopardi, "Droplet Deposition and Interchange in Annular Gas-Liquid Flow," UKAEA Rept. AERE-R10147 (1981).

Ardron, K. H. and P. C. Hall, "Droplet Hydrodynamics and Heat Transfer in the Dispersed Flow Regime in Bottom Flooding," C.E.G.B. Report R.D. 1B15007N81 (1981).

Clamen, A., and W. H. Gauvin, "Effects of Turbulence on the Drag Coefficients of Spheres in a Supercritical Flow Regime," *AIChE J.*, **15**, 184 (1969).

Clift, R., and W. H. Gauvin, *Proc. Chemecor '70*, **1**, 14 Australia (Aug., 1970).

———, "Motion of Entrained Particles in Gas Streams," *Can. J. Chem. Eng.*, **49**, 430 (1971).

Clift, R., J. R. Grace, and M. E. Weber, *Bubbles, Drops, and Particles*, Academic Press, New York (1978).

Cousins, L. B., and G. F. Hewitt, "Liquid Phase Mass Transfer in Annular Two-Phase Flow: Droplet Deposition and Liquid Entrainment," UKAEA Rept. AERE-R5657, (1968).

Dryden, H. L., G. B. Schubnner, W. G. Mork, and H. K. Skramstud, *NACA Repts.* 581 (1937).

James, P. W., G. F. Hewitt and P. B. Whalley, "Droplet Motion in Two-Phase Flow," UKAEA Report, AERE-R9711, (1980).

Kada, H., and T. J. Hanratty, "Effects of Solids on Turbulence in a Fluid," *AIChE J.*, **4**, 624 (1960).

Langner, H., and F. Mayinger, "Tropfenspektrum und Entrainment in Geheizten Damppf-Flüssigkeits-Gemischen," **16**, 23 (1982).

Lopes, J. C. B., and A. E. Dukler, "Droplet Entrainment in Vertical Annular Flow and Its Contribution to Momentum Transfer," *AIChE J.*, **32**, 1500 (1986).

Lumley, J., "Some Problems Connected with the Motion of Small Particles in Turbulent Fluid," Ph.D. Diss. John Hopkins Univ., Baltimore (1957).

Marchildon, E. K., and W. H. Gauvin, "Effects of Acceleration, Deceleration and Particle Shape on Single-Particle Drag Coefficients in Still Air," *AIChE J.*, **25**, 938 (1979).

Neve, R. S., "The Importance of Turbulence Macroscale in Determining the Drag Coefficient of Spheres," *Int. J. Heat Fluid Flow*, **7**, 28 (1986).

Odar, F., and W. S. Hamilton, "Forces on a Sphere Accelerating in a Viscous Fluid," *J. Fluid Mech.*, **18**, 302 (1964).

Rudinger, G., "Penetration of Particles Injected into a Constant Cross Flow," *A.I.I.A. J.*, **12**, 1138 (1974).

Schlichting, H., "Boundary-Layer Theory," McGraw-Hill, New York (1979).

Semiat, R., and A. E. Dukler, "Simultaneous Measurements of Size and Velocity of Bubbles or Drops: A New Optical Technique," *AIChE J.*, **27**, 148 (1981).

Tatterson, D. F., "Rates of Atomization and Drop Size in Annular Two-Phase Flow," Ph.D. Diss., Univ. Illinois (1975).
Taylor, G. I., "Statistical Theory of Turbulence. V: Effect of Turbulence on the Boundary Layer. Theoretical Discussion of Relationships Between Scale of Turbulence and Critical Resistance of Spheres," *Proc. Roy. Soc., London,* **156A,** 307 (1936).
Temkim, S., and H. K. Mehta, "Droplet Drag in an Accelerating and Decelerating Flow," *J. Fluid Mech.,* **116,** 297 (1982).
Tong, A. W., and L. E. Hochreiter, "Entrained Droplet Sizes, Distribution and Velocities in Dispersed Flow Film Boiling," ASME/ISME Meeting, Hawaii (1983).
Torobin, L. B., and W. H. Gauvin, "The Drag Coefficients of Single Spheres Moving in Steady and Accelerated Motion in a Turbulent Fluid," *AIChE J.,* **7,** 615 (1961).
Ueda, T., "On the Droplets Entrained in Two-Phase Annular and Mist Flow," *Two-Phase Flow Dynamics,* ed. Bergles, Hemisphere Press, (1981).
Uhlherr, P. H. T., and C. G. Sinclair, *Proc. Chemeca '70,* **1,** 1 Australia (Aug., 1970).
Wilkes, N. S., B. J. Azzopardi, and I. Willets, "Drop Motion and Deposition in Annular Two-Phase Flow," *Proc. Nuclear Reactor Thermal-Hydraulics,* **1,** 202, Am. Nuclear Soc. (1983).
Yeoman, M. L., B. J. Azzopardi, H. A. White, C. J. Bates, and P. J. Robert, "An Optical Development and Application of a Two-Color LDA System for the Simultaneous Measurement of Particle Size and Particle Velocity," UKAEA Report AERE-R10468 (1982).
Zabaras, G., "Studies of Vertical Annular Gas-Liquid Flows," Ph.D. Diss. Univ. Houston, TX (1985).
Zabaras, G., A. E. Dukler, and D. M. Maron, "Vertical Upward Cocurrent Gas-Liquid Annular Flow," *AIChE J.,* **32,** 829 (1986).

Manuscript received July 29, 1986, and revision received Jan. 5, 1987.